Available online at www.sciencedirect.com

ScienceDirect

Icarus 194 (2008) 53–64

ICARUS

www.elsevier.com/locate/icarus

Observations of atmospheric water vapor above the Tharsis volcanoes on Mars with the OMEGA/MEx imaging spectrometer

Luca Maltagliati [a,*], Dmitry V. Titov [a,b], Thérèse Encrenaz [c], Riccardo Melchiorri [c], Francois Forget [d], Maya Garcia-Comas [a], Horst U. Keller [a], Yves Langevin [e], Jean-Pierre Bibring [e]

[a] *Max-Planck-Institut für Sonnensystemforschung, Max-Planck Str. 2, 37191 Katlenburg-Lindau, Germany*
[b] *Space Research Institute (IKI), Profsojuznaja 84/32, 117810 Moscow, Russia*
[c] *Observatoire de Paris, DESPA Place Jules Janssen, 92195 Meudon, France*
[d] *LMD/CNRS/Université Paris VI, 4 Place Jussieu, 75252 Paris, France*
[e] *IAS/CNRS/Université Paris XI, Bat 121, 91405 Orsay, France*

Received 6 April 2007; revised 10 September 2007

Available online 6 November 2007

Abstract

The OMEGA imaging spectrometer onboard the Mars Express spacecraft is particularly well suited to study in detail specific regions of Mars, thanks to its high spatial resolution and its high signal-to-noise ratio. We investigate the behavior of atmospheric water vapor over the four big volcanoes located on the Tharsis plateau (Olympus, Ascraeus, Pavonis and Arsia Mons) using the 2.6 µm band, which is the strongest and most sensitive H_2O band in the OMEGA spectral range. Our data sample covers the end of MY26 and the whole MY27, with gaps only in the late northern spring and in northern autumn. The most striking result of our retrievals is the increase of water vapor mixing ratio from the valley to the summit of volcanoes. Corresponding column density is often almost constant, despite a factor of ∼5 decrease in air mass from the bottom to the top. This peculiar water enrichment on the volcanoes is present in 75% of the orbits in our sample. The seasonal distribution of such enrichment hints at a seasonal dependence, with a minimum during the northern summer and a maximum around the northern spring equinox. The enrichment possibly also has a diurnal trend, being the orbits with a high degree of enrichment concentrated in the early morning. However, the season and the solar time of the observations, due to the motion of the spacecraft, are correlated, then the two dependences cannot be clearly disentangled. Several orbits exhibit also spatially localized enrichment structures, usually ring- or crescent-shaped. We retrieve also the height of the saturation level over the volcanoes. The results show a strong minimum around the aphelion season, due to the low temperatures, while it raises quickly before and after this period. The enrichment is possibly generated by the local circulation characteristic of the volcano region, which can transport upslope significant quantities of water vapor. The low altitude of the saturation level during the early summer can then hinder the transport of water during this season. The influence of the coupling between atmosphere and surface, due mainly to the action of the regoliths, can also contribute partially to the observed phenomenon.
© 2007 Elsevier Inc. All rights reserved.

Keywords: Mars, atmosphere; Mars, climate; Infrared observations; Spectroscopy

1. Introduction

The Tharsis Bulge is the most evident and extensive signature of the past volcanic activity on Mars. The region as a whole is 3–4 km over the zero datum, and it contains four huge shield volcanoes. Olympus Mons, on the north-western edge of Tharsis, is ∼21 km tall and ∼600 km wide at the base. The other three (Ascraeus, Pavonis and Arsia Montes), which cross all the area in latitude on an oblique line from north-east to south-west, are slightly shorter (Ascraeus, 18 km; Pavonis, 14 km; Arsia, 19 km) and 400 km wide on average.

Many observations in the last thirty years show that the atmosphere in the vicinity of the volcanoes is particularly active. The information that the flanks and summit of the volcanoes are a favorite location for the formation of water ice clouds comes

* Corresponding author.
E-mail address: maltagliati@mps.mpg.de (L. Maltagliati).

0019-1035/$ – see front matter © 2007 Elsevier Inc. All rights reserved.
doi:10.1016/j.icarus.2007.09.027

already from the pre-Viking era (Hartmann, 1978). Clouds over volcanoes show both diurnal (Hunt et al., 1980) and seasonal (Benson et al., 2003) trends, with little interannual variations (Benson et al., 2006). The clouds form mainly in the northern spring and summer, with the peak at $L_s \sim 100°$ and few differences between the volcanoes, Arsia being the only one with a nearly continuous cloud activity. Clouds can be considered the signature of a significant local circulation in the vicinity of the volcanoes. In the mesoscale model of Michaels et al. (2006), this local circulation is the product of a symbiosis between two mechanisms: the thermally-induced flows due to low thermal inertia volcanoes, and mountain gravity waves, of which lee-waves are one manifestation. The result is an effective pumping mechanism that transports atmospheric material—dust, water vapor, aerosols—both vertically and horizontally, and can influence the atmosphere and the climate even to global scales. Due to the importance of local topography in the triggering of this circulation, such an unified view can be obtained only in the framework of mesoscale circulation models. The typical grid cell dimension of current Global Circulation Models is not fine enough to resolve specific surface features as the volcanoes. Current GCMs, thus, are poorly suited to investigate these local phenomena.

In contrast to this richness of information about cloud activity, only sparse observations focusing on the behavior of water vapor above the volcanoes exist. The only extensive and dedicated study was carried out by Titov et al. (1994) using the ISM instrument onboard the Phobos-2 spacecraft. ISM was an infrared mapping spectrometer working on the reflected spectrum (0.7–3.2 μm), with high signal-to-noise ratio and fairly good spatial resolution (5–20 km). These observations indicated significantly higher water vapor mixing ratio above the volcanoes, compared to the surrounding terrain. This peculiar water vapor anomaly on the volcanoes was considered to be the evidence for an enhanced exchange between atmosphere and surface, due to higher adsorptive capabilities of the regolith on the volcanoes than on the surrounding terrain. Titov et al. (1994) presented two regolith–atmosphere exchange models that considered respectively the influence of the variations in mineralogical composition and in thermal inertia. Both effects can explain the water vapor anomaly, separately or in combination.

Results from the other instruments are more ambiguous. The Viking Mars Atmospheric Water Detector (MAWD) found that the water vapor abundance divided by airmass has a maximum in the Tharsis region (Jakosky and Farmer, 1982, Fig. 8b). From this, the authors concluded that the water vapor mixing ratio is not constant, but instead depends on altitude. Moreover, MAWD high spatial resolution data show indications of a water anomaly in the Tharsis region (Farmer et al., 1977). The Thermal Emission Spectrometer (TES) onboard the Mars Global Surveyor found high scaled column density on the Tharsis region, but not on the volcanoes themselves (Smith, 2002). Compared to these instruments, ISM had the advantage of being the only one, up to now, with sufficiently high spatial resolution and signal-to-noise ratio to map the volcanoes in detail. The ISM-Phobos instrument had however two significant limiting factors: the low spectral resolution, that left only one spectral point for the water vapor band analysis, and an uncertainty of 10% on the absolute calibration.

The Mars Express mission provides new opportunities to study atmospheric water on Mars with several spectrometers (Encrenaz et al., 2005; Fedorova et al., 2006; Melchiorri et al., 2007). In this paper we present the results of a detailed analysis of the behavior of water vapor using an improved successor of ISM, the OMEGA infrared mapping spectrometer, which has been acquiring data since the beginning of 2004. In particular, we focus on the atmospheric water behavior in the vicinity of the Tharsis volcanoes. In Section 2 we present the OMEGA instrument and the data sample that we analyzed. The reduction technique is described in Section 3. Then, in Sections 4 and 5 we present the results and subsequent discussion.

2. Instrument and dataset

The mapping spectrometer OMEGA (Observatoire pour la Minéralogie, l'Eau, les Glaces et l'Activité), onboard the Mars Express spacecraft, operates in the spectral range 0.38–5.1 μm, divided in three channels: visible and near-IR (VNIR channel, between 0.38 and 1.05 μm) and two short wavelength IR ranges (SWIR-C, between 0.93 and 2.73 μm, and SWIR-L, which covers the interval 2.55–5.1 μm). In our analysis we use the SWIR-C channel, made up by 128 spectral points (*spectels*), whose technical characteristics are summarized in Bibring et al. (2004). We recall here that OMEGA's main strength is, in addition to its mapping capability, the combination of high spatial resolution (1–2 km on average) with high signal-to-noise ratio ($S/N > 100$ over the whole spectral range), which allows to study variations of atmospheric trace gases and surface minerals in an unprecedented detail. Indeed, OMEGA has twice the spectral resolving power and an instantaneous field-of-view (IFOV) almost 3 times higher compared to ISM-Phobos. The declared accuracy of the relative calibration is better than 1%.

Fig. 1 shows an example of the SWIR-C spectrum. The three arrows indicate the water vapor bands present in this channel. Between them, we chose the band at ∼2.6 μm for the water vapor retrieval. Despite being slightly blended in the red wing with the 2.7 μm CO_2 band, in fact, this band is the most favorable because it is free of mineralogic features and 3–5 times stronger than the other two. Moreover, we performed a series of numerical tests that prove that this band is also the most sensitive to water vapor amount. On the contrary, the 1.9 μm band is almost insensitive to mixing ratio, while the 1.38 μm one is better than the latter but more affected by aerosols and by the eventual presence of water ice, which has a strong signature at 1.5 μm.

The OMEGA dataset available up to the beginning of 2006 covers more than one martian year, from $L_s = 330.1°$ MY26 to $L_s = 358.4°$ MY27. In total 41 orbits, out of around 650, fly over one of the four Tharsis mountains. We included also the orbits that passed over the flanks of the volcanoes. Fig. 2 shows the seasonal and local time coverage of the sample. The orbits cover more or less smoothly all the martian year with two main gaps, between $L_s = 60°$ and $L_s = 90°$ (late north-

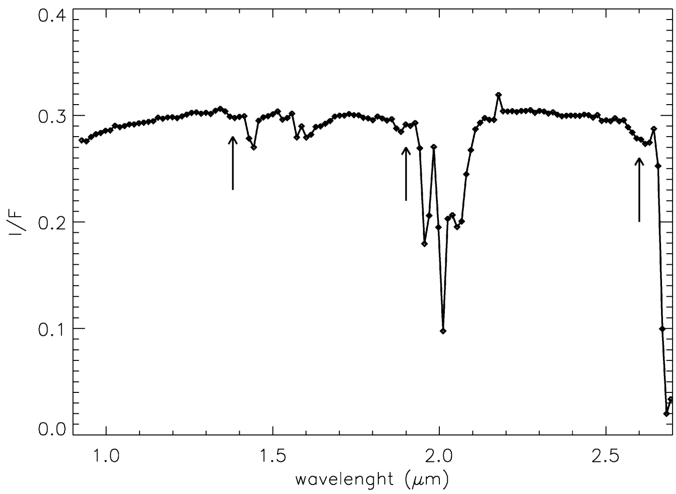

Fig. 1. Example of spectrum of the SWIR-C channel of OMEGA (Orbit 37_3, latitude = 25.1° N, longitude = 227.2° E). The three arrows point out the three water vapor bands present in this wavelength range. The most evident signatures of the spectrum, at 1.42, 2 and 2.7 μm, are due to CO_2. The diamonds indicate the exact OMEGA spectral grid points.

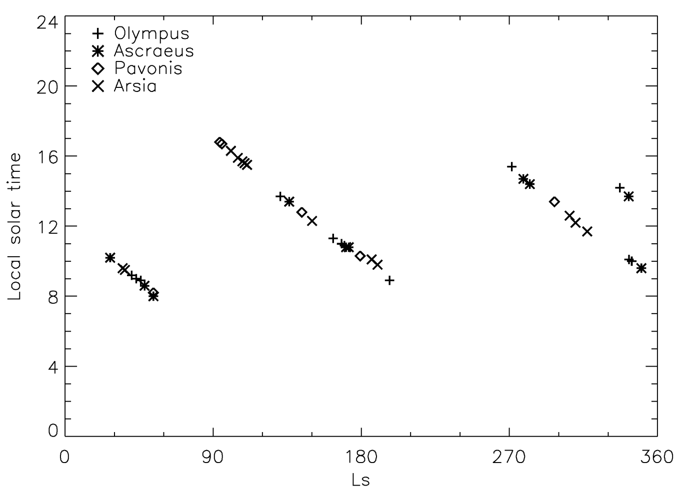

Fig. 2. Seasonal and local time coverage of the Tharsis volcanoes in the OMEGA observations.

ern spring) and $L_s = 200°$ and $L_s = 270°$ (almost the whole northern autumn). The local hour of the observation is dependent on the season due to the evolution of Mars Express orbit, but the whole sample includes all times between 8 in the morning and 17 in the afternoon, albeit at different seasons. All the four volcanoes have a good coverage: 12 orbits cover Olympus Mons, 10 Ascraeus Mons, 6 Pavonis Mons and 13 Arsia Mons. As we can see from Fig. 2, even the less observed mountain, Pavonis, has at least one orbit per season.

3. Data reduction

We employ a minimization procedure which fits the absolute measured OMEGA spectrum in the 2.6 μm water vapor band with a synthetic one. The synthetic spectrum is built by the fast and accurate algorithm of atmospheric transmittance calculation described in Titov and Haus (1997), taking into account the OMEGA spectral response and the atmospheric pressure and temperature at the location of interest. The only free parameter in our best-fit retrieval is the water vapor volume mixing ratio which is assumed constant below the saturation level. This approach is different from the method of ratioed spectra, used, for instance, by Encrenaz et al. (2005). The use of the absolute spectrum avoids any systematic uncertainties related to the choice of the reference spectrum that is required in the ratioed spectra method, such as mineralogic spectral features, or residual atmospheric contributions. However, it retains the sources of uncertainty related to the instrument itself, as the precision of the spectral calibration and of the OMEGA transfer function. These effects are considered in detail in Section 3.4.

3.1. Computation of the synthetic spectrum

We calculate the synthetic spectrum using a line-by-line procedure which takes into account the contribution of atmospheric CO_2 and H_2O. Following Titov and Haus (1997), the monochromatic absorption cross-section per molecule $k(p, T, \nu)$ of an atmospheric constituent can be written as

$$k(p, T, \nu) = pF(T, \nu), \tag{1}$$

where p is the pressure in bar, and $F(T, \nu)$ is the function of temperature and wavenumber which describes the contribution of the lines to absorption at wavenumber ν. The values of the function $F(T, \nu)$ are obtained by interpolation over T of the look-up table $F(T_i, \nu_j)$, precalculated using the line-by-line code. The spectral parameters are taken from the HITRAN2004 database (Rothman et al., 2005). For each ν, the total monochromatic opacity $\tau(\nu)$ is given by

$$\tau(\nu) = \sum_{\text{gas}} \tau_{\text{gas}}(\nu), \tag{2}$$

where

$$\tau_{\text{gas}}(\nu) = 10^6 \frac{N_A}{g\langle M\rangle} \int_{p_0}^{0} F_{\text{gas}}(T, \nu) p f_{\text{gas}} \, \mathrm{d}p, \tag{3}$$

where N_A is the Avogadro number, g the gravity acceleration, $\langle M\rangle$ the mean molecular weight of the martian atmosphere, p_0 the surface pressure, and f_{gas} the mixing ratio of each gaseous component included in the synthetic spectrum, in our case H_2O and CO_2. Pressure, temperature and mixing ratio of water vapor are functions of altitude z, while the mixing ratio of CO_2 is considered to be constant throughout the atmosphere and it can be taken out of the integral. All the units are in the cgs system but the pressure which is in bar.

The monochromatic transmittance $tf(\nu)$ is

$$tf(\nu) = \exp\big[-\tau(\nu)AM\big], \tag{4}$$

where AM is the air mass. Finally, the monochromatic transmittance is convolved with the OMEGA spectral response R_Ω so that the synthetic spectrum ST for a spectel at wavenumber ν_0 is

$$ST(\nu_0) = \int tf(\nu) R_\Omega(\nu - \nu_0) \, \mathrm{d}\nu. \tag{5}$$

We neglect atmospheric dust and aerosols in the synthetic spectrum calculation.

3.2. Climatological parameters

The synthetic spectrum strongly depends on the climatological parameters: pressure, temperature and water vapor vertical profiles, and the dust and aerosol scenario. Unfortunately, a comprehensive dataset of these characteristics and their temporal dependence does not exist, especially for such a specific environment as the volcanoes. Simultaneous observations of the temperature structure on the volcanoes by PFS-MEx lack sufficient spatial resolution and seasonal coverage (Grassi et al., 2005). Thus, we extract these parameters from the European Martian Climate Database (EMCD, version 4.1), which relies on the General Circulation Model described in Forget et al. (1999). For the given spatial and temporal coordinates and dust scenario, our program extracts temperature and pressure values from EMCD from the surface up to $\sim$110 km, with the vertical step decreasing near the surface. For the dust scenario we chose the "Martian Year 24" reference, which is considered typical by EMCD. The main problem linked to the use of EMCD is its low spatial resolution. The model has a longitude–latitude grid of $5.675° \times 3.75°$, much coarser than the OMEGA spatial resolution. This can significantly affect the surface pressure determination, especially in the vicinity of the volcanoes due to the extreme topographic variations. In order to overcome this problem we used the *pres0* procedure provided by EMCD, which computes the surface pressure p_0 at the finest MOLA resolution (1/32°). Then we scaled the whole pressure profile to this new value. EMCD does not include an equivalent routine for the temperature, so such a correction is not possible for the temperature profile. This approximation does not influence too much the spectrum itself, because we are looking at the reflected part of the spectrum, which is independent of temperature at first order. Moreover, on Mars the surface temperature is only weakly dependent on the elevation, so EMCD low spatial resolution is still acceptable. Nevertheless, the temperature profile plays an important role for the computation of the height of saturation level (see below). The uncertainty due to temperature will be discussed in detail in Section 3.4.

The last climatological parameter we have to consider is the vertical distribution of water vapor. Also in this case, the observational data are very sparse (Titov, 2002) and had never been related to the vicinity of volcanoes. Experiments suggest that water vapor is uniformly mixed in the lower part of the atmosphere. The thickness of this layer is correlated with the altitude of the condensation level, which is quite high (20–25 km) in the early northern spring and very close to the surface during the aphelion period (see Fig. 5 in Titov, 2002). Condensation occurs when the partial pressure of water p_{H_2O} becomes equal to the saturation pressure e_s (Fig. 3, left panel). At a very good approximation, the saturation pressure depends only on temperature, thus the height in the atmosphere z_{sat} where the saturation regime starts can be found from

$$e_s\big(T(z_{sat})\big) = f_{H_2O}(z_{sat})\,p(z_{sat}). \qquad (6)$$

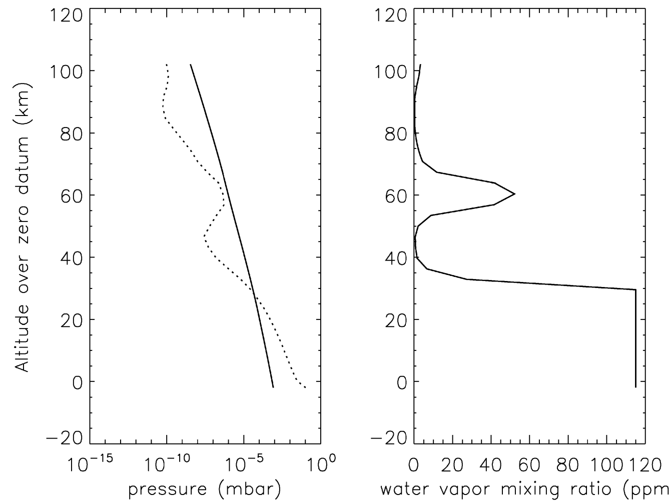

Fig. 3. (Left) Example of vertical profiles of the water vapor partial pressure (solid line) and of the saturation pressure (dotted line). The crossing point of the two lines defines the height of the saturation level z_{sat}. (Right) Corresponding vertical profile of water vapor.

If we consider the water vapor well mixed below the saturation level, we just need to know the temperature and pressure profiles and the explicit relation between the saturation pressure and temperature. In our case the first two come from EMCD, while for the third we used the experimental results of Mauersberger and Krankowsky (2003). Since no experimental data for the saturation pressure below 164.5 K exist, we extend the validity of Eq. (2) in Mauersberger and Krankowsky (2003) for $T \leqslant 169$ K.

Our vertical profile of water vapor $f(z)$ is then composed of two parts. Below the saturation level, we employ a constant mixing ratio f_{H_2O}, while the upper part follows the saturation curve (Fig. 3, right panel). Above the saturation level, water vapor mixing ratio falls rapidly to zero. The apparent "wet layer" between $\approx$55–65 km is due to the temperature inversion present at those altitudes, which increases the saturation pressure (as the dotted line of the left panel of Fig. 3 shows). Consequently, the ratio between saturation pressure and partial pressure increases, as does the mixing ratio. This wet layer, which has never been observed and whose existence is unlikely, has no influence on our results.

The vertical profile described above includes only the physics of condensation, neglecting any net effect due to advection from the surface, precipitation of condensed water particles, and eddy mixing. This approximation is validated by several measurements, which indicate that the vertical distribution of water vapor is dominated by saturation processes (Gurwell et al., 2000; Encrenaz et al., 2001), and it has the advantage that it does not rely on the hypotheses of a specific model. We tested the influence of the H_2O vertical profile on our retrievals with some runs employing three other profiles:

(1) vapor confinement in the first 3 km of the atmosphere (roughly corresponding to the boundary layer), simulating an extreme case of surface–atmosphere coupling with no vertical mixing;

(2) vapor mixing ratio decreasing linearly by a factor of 10 from the surface to the saturation level, a case similar to the previous one with the inclusion of an inefficient eddy mixing;
(3) vapor mixing ratio increasing linearly by a factor of 10 from the surface to the saturation level, which accounts for a strong precipitation of condensed particles with negligible advection from the surface.

This test shows that the assumption regarding the H_2O vertical profile significantly affects the retrieved mixing ratio. In the second and third case, the column density of water vapor and the average value of the mixing ratio below the saturation level increase and decrease by ∼20%, respectively. The first case is the most extreme, and results in the doubling of mixing ratio and the halving of column density. However, all the retrieved maps are very similar, with no qualitative discrepancy between the different profiles. This means that the relative difference between the summit of the volcano and its bottom, which is the focus of Sections 4 and 5, is only weakly dependent on the vertical distribution.

3.3. *The measured spectrum and the fitting procedure*

The raw OMEGA data is first treated with a standard procedure to eliminate the first-order instrumental contributions (flatfielding, radiometric calibration, photometric function). After that, we divide the result by the solar spectrum, convolved with the OMEGA spectral response. The spectra are then binned in latitude and longitude.

The binning procedure has the function to clean the data from random noise and to speed up the time-consuming computations of the synthetic spectra for each loop step in the best-fit procedure. The high S/N ratio guarantees that only a small number of spectra is needed to get rid of noise-related fluctuations, even in the case of volcanoes where the atmospheric bands are weaker. Thus, the choice of the number of spectra to be binned is mainly determined by computational issues. In the binning process we tried to maintain approximately the same spatial resolution between the orbits. Since the resolution varies with the distance of the spacecraft from the planet, the number of binned spectra depends on the orbit. In approximately 20% of cases the spacecraft is so close to the pericenter (width of the OMEGA swath $<0.2°$) that we decided to make only a 1D latitudinal retrieval, without employing the OMEGA mapping capability. The spatial resolution of all these orbits is $<0.15°$ after binning. Around 40% of the rest of the orbits have spatial resolution (both in latitude and in longitude) better than 0.2°, and for ∼75% the spatial resolution is $<0.3°$. On average, after the binning we have ∼400 spectra for each orbit, but the actual number varies a lot, from around 900 spectra in the orbits with high coverage down to ∼60 spectra for the retrievals close to the pericenter of the spacecraft.

Finally, we normalize the binned measured spectrum to its continuum. Fig. 4 shows an example of a measured spectrum after binning and normalization. The choice of continuum, however, is not straightforward, because the 2.6 μm band is blended

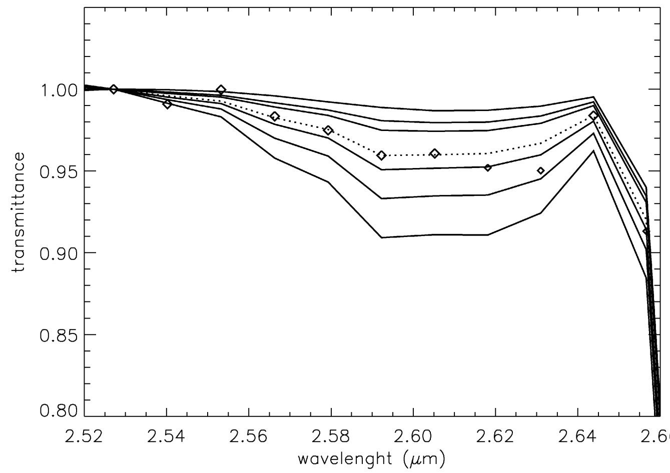

Fig. 4. OMEGA spectra in the 2.6 μm H_2O band: the measured OMEGA spectrum (diamonds) and the synthetic spectra (solid lines) calculated for different water vapor mixing ratios (10, 50, 100, 500, 1000 and 2000 ppm, top to bottom). The dotted line marks the best-fit synthetic spectrum, for 320 ppm. In this best-fit, the mean absolute deviation of the transmittance between the measured and the synthetic spectrum is $\sigma_{\text{best}} = 1.82 \times 10^{-3}$. The smaller diamonds indicate those spectels that are not used for the retrieval (see text). All the spectra in this plot are arbitrarily normalized to the leftmost spectel.

in the red wing with the strong CO_2 2.7 μm band (Fig. 1). Thus, we have to take into account the contribution from both gases. The continuum reference points are the 2.644 μm spectel in the red wing, and an average between the three spectels at 2.527, 2.540 and 2.553 μm for the blue wing (Fig. 4). The continuum between these spectels is then computed with a simple linear interpolation. The continuum in the reference spectels is adjusted at each iteration according to the current value of mixing ratio, in order to take into account the residual H_2O and CO_2 absorption at these wavelengths.

We determine the best-fit by minimizing the mean absolute deviation (σ) between the synthetic and the measured spectrum in the seven spectels between 2.527 and 2.605 μm, indicated with bigger diamonds in Fig. 4. The two spectels at 2.618 and 2.631 μm, in the right wing of the band, cannot be used in an automatic minimization procedure because of instrumental issues. The only parameter that changes in the minimization loop is the volume mixing ratio of water vapor below the saturation level, f_{H_2O}. The water vapor column density W corresponding to the retrieved mixing ratio profile is then computed using the integral

$$W = \frac{1}{g} \frac{m_v}{\langle M \rangle} \int_0^{p_0} f_{H_2O}(p)\, dp, \tag{7}$$

where m_v is the molecular weight of water vapor, and $f_{H_2O}(p)$ is the mixing ratio at pressure p. The mean absolute deviation of the best-fit σ_{best} gives a measure of the goodness-of-fit (GOF) for each point. Mapping the GOF for each orbit allows us to visualize the retrieval quality and its spatial dependence. A best-fit is considered good when $\sigma_{\text{best}} \lesssim 6.5 \times 10^{-3}$. We always get good quality fits in our sample, except a portion of two orbits—a strip in orbits 2483 (MY = 27, $L_s = 342.7°$) and 2494 (MY = 27, $L_s = 344.3°$)—probably due to a temporary instrumental effect because it is in the same line for both orbits. These portions were excluded from our analysis.

3.4. Retrieval uncertainties

The possible error sources in our retrievals are: the uncertainties on the climatological parameters, pressure and temperature; the influence of ice clouds and aerosols, which are not included in the computation of our synthetic spectrum; instrumental noise and calibration uncertainties; and eventual small-scale atmospheric fluctuations, which are smoothed out due to the binning. Here we analyze the individual contribution of each uncertainty to the error in mixing ratio, which is our fitting parameter.

The uncertainty in pressure determination is mainly due to EMCD low spatial resolution. This effect on the surface pressure is limited, because we use the EMCD procedure *pres0*, which employs high resolution MOLA data. We suppose that the EMCD pressure profile scaled to the surface pressure given by *pres0* well approximates the pressure profile on the volcanoes. The associated relative error on mixing ratio is of a few percent, which is negligible compared to the other error sources.

An estimate of the uncertainty due to temperature is more complex. In this case, there is no correction equivalent to *pres0*, and the effects of EMCD low spatial resolution are difficult to quantify. The temperature profiles retrieved on the volcanoes by PFS, which are the only measurements we can compare the model with, have significant uncertainties below 5 km (Grassi et al., 2005), where most of the atmospheric water resides. A test-run for Olympus Mons with a higher latitudinal resolution of 1.35° (not fully implemented on EMCD yet) at $L_s = 0°$ and LST 3 P.M. hints that the difference in surface temperature on the volcanoes is $\sim$5–10 K, and only a few K on the plains. An additional contribution to the temperature uncertainty comes from the dust loading assumed in our procedure. The use of the EMCD "Martian Year 24" scenario is supported by the absence of major dust storms over the Tharsis region during our observations, and we can estimate the corresponding temperature uncertainty of few K. In order to estimate its influence on the retrievals, we made a number of tests translating the whole temperature profile by ± 3, 5, 10 and 13 K. The results depend almost exclusively on the near-surface temperature. If the near-surface temperature is low, the saturation level is closer to the surface and the retrieval is more sensitive to the temperature uncertainty. Conversely, a higher temperature means a higher saturation level and the band is less sensitive to temperature changes. The mixing ratio error due to temperature has thus a complicated pattern which depends on season, time of the day and spatial position, with no clear trends. As an indicative value, we can consider a relative error of 30% on mixing ratio due to temperature uncertainties.

Dust opacity also affects the band depth. Fedorova et al. (2004) studied this effect in detail, reanalyzing the MAWD–Viking observations with the inclusion of a radiative transfer code with multiple scattering. The presence of dust would influence the retrieval in the valley more than on the top of the volcanoes due to the greater opacity, thus leading to a systematic effect. However, the results of Fedorova et al. (2004) show that significant changes are obtained only when the opacity of the atmosphere is much higher than the typical atmospheric state (i.e., during dust storms), and for high airmasses. Moreover, the extinction due to dust at 2.6 µm is smaller than at 1.38 µm, the wavelength of the water vapor band used by MAWD. In conclusion, we believe that the influence of dust on our retrievals can be neglected.

Another atmospheric phenomenon that can introduce spurious features in the retrieval and influence the water vapor band is the presence of water ice clouds. This is a particularly delicate issue in the Tharsis region, a favorite location for the formation of ice clouds. In fact, an ice-cloud layer ubiquitously present only over the lower part of the volcanoes would both deplete the atmosphere of water vapor and mask the residual water vapor laying underneath, while the top of the volcanoes, standing over the clouds, would not be affected. We now explain why the presence of ice clouds does not greatly affect our results. We mapped the depth of the 1.5 µm water ice band, using the same binning as for the water vapor retrievals. Fig. 5 shows examples of water ice maps of the same orbits used for H_2O mixing ratio retrievals and presented in the next section (Figs. 6 and 7). Figs. 5a and 5b have no signature of ice cloud; Fig. 5c shows the volcano surrounded by a cloud up to 9–11 km altitude, while the top is cloud-free; lastly, Fig. 5d exhibits an intermediate situation, with a band depth of 2–3% in the north-western part of the orbit, probably not a completely formed cloud but just a faint haze. The map of the ice band, however, does not correlate with the mixing ratio distribution: even those orbits with a clear signature of ice clouds exhibit no peculiar behavior compared to the orbits in the same season and without clouds. Most orbits in our data sample show no clouds (ice band depth $\leqslant$2%) or just a thin haze (band depth 2–3%). The influence of water ice on our sample is thus limited, and the error on mixing ratio due to the presence of ice clouds is minor compared to the other contributions.

The last group of uncertainties affects the counts of the individual spectels, and includes the effects of instrumental noise, the precision of OMEGA calibration and the binning procedure. The standard deviation from the mean for each spectel inside the binning domain is always close to 1%, which is incidentally also the relative calibration precision. Thus, we made a series of test retrievals on synthetic spectra created superimposing a random value within 1% to each spectel. The relative error on mixing ratio ranges from $\sim$10% on the plains to $\sim$30% on the mountains. This is an expected trend because, due to pressure effects, the band becomes shallower going from the valley to the top of the volcanoes, and thus more sensitive to the spectel fluctuations.

To sum up, the main contributions to the error are the temperature uncertainty and the noise of individual spectels. If we consider these two sources of error independent from each other, we can compute the total error on mixing ratio as the quadratic sum, which is $\sim$30% on the plains and $\sim$40% on the volcanoes.

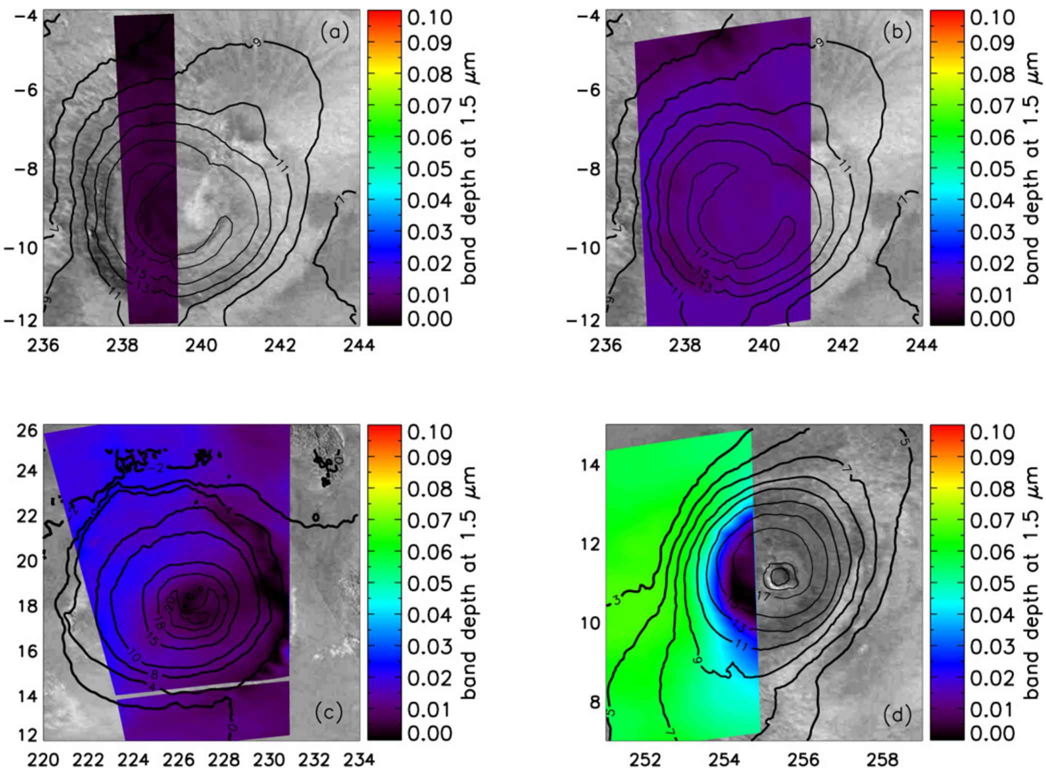

Fig. 5. Four examples of 1.5 μm water ice band depth maps. (a) Arsia Mons, orbit 424, $L_s = 36.4°$, local time = 9:30 A.M.; mixing ratio map shown in Fig. 6. (b) Orbit 413 over Arsia Mons, $L_s = 35.0°$, solar time = 9:30 A.M.; mixing ratio map shown in Fig. 7. (c) Olympus Mons, orbit 501, $L_s = 46.0°$, solar time = 8:55 A.M.; mixing ratio map in Fig. 7. (d) Ascraeus Mons, orbit 563, $L_s = 53.7°$, local time = 8:00 A.M.; mixing ratio map shown in Fig. 6. The x and y axes of each plot are respectively longitude and latitude.

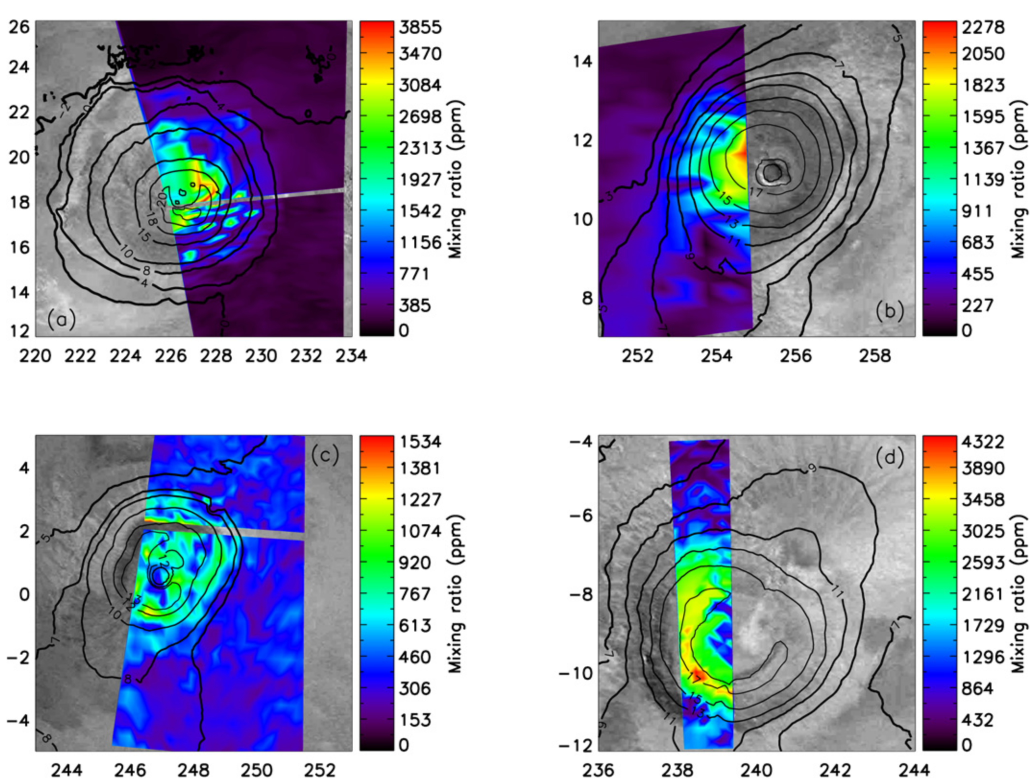

Fig. 6. Maps of H_2O mixing ratio retrieved on the four Tharsis volcanoes, superimposed on the Viking images and on the MOLA/MGS altitude level curves. (a) Olympus Mons, orbit 479, $L_s = 43.3°$, local time = 9:00 A.M. (b) Ascraeus Mons, orbit 563, $L_s = 53.7°$, local time = 8:00 A.M. (c) Pavonis Mons, orbit 1510, $L_s = 179.3°$, local time = 10:20 A.M. (d) Arsia Mons, orbit 424, $L_s = 36.4°$, local time = 9:30 A.M.

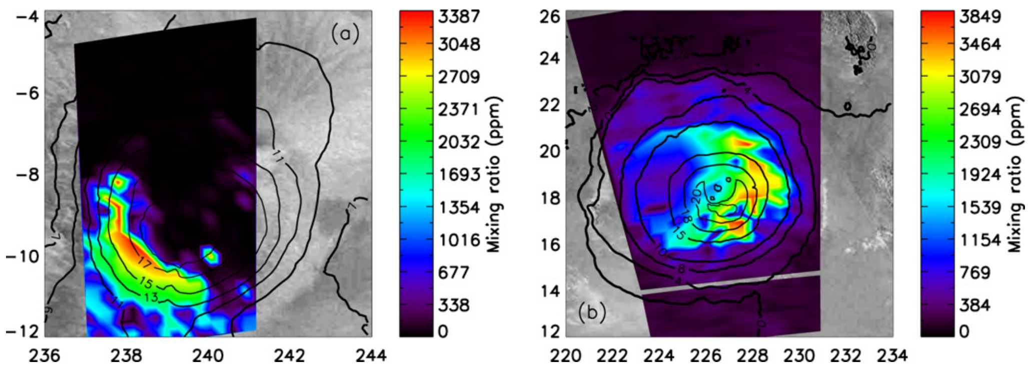

Fig. 7. Examples of strong enrichment structures. (a) Orbit 413 over Arsia Mons ($L_s = 35.0°$, solar time = 9:35 A.M.). (b) Orbit 501, Olympus Mons ($L_s = 46.0°$, solar time = 8:55 A.M.).

4. Results

4.1. Water vapor mixing ratio

First, we present the results of the mixing ratio retrievals below the saturation level. Fig. 6 shows four examples of mixing ratio maps on the volcanoes at different times of the day and seasons. All of them share a common behavior: the mixing ratio of water vapor increases from the valley to the summit, indicating an enhancement of H_2O over the mountains. This enrichment is the most peculiar behavior of water vapor in the atmosphere over the volcanoes. In order to quantify it, we computed for each orbit the mean mixing ratio on the lower part of the volcano (f_{bottom}) and on its summit (f_{top}). The ratio $f_{\mathrm{top}}/f_{\mathrm{bottom}}$ gives an estimate of the bulk enrichment of water vapor on the volcano. The altitude level that divides the two regions is set at 8–10 km, depending on the volcano. It must be remarked that this enrichment ratio is not always a good proxy for the actual degree of enrichment on the volcano, especially when significant spatial inhomogeneities in mixing ratio distribution are present. Fig. 7 displays two examples of such enrichment structures. Fig. 7a, in particular, shows that Arsia Mons is not particularly enriched compared to the valley nearby, but there is a strong crescent-shaped structure on the south-western flank. In these cases a simple average over altitude can mask the real degree of enrichment. We consider the structures as a sign of water enhancement on the volcano, so we included these orbits in the enriched group even when their bulk enrichment ratio is low.

The enrichment pattern varies from orbit to orbit. For example, in Fig. 6 only the higher part of Pavonis Mons is enriched, without the progressive increase of mixing ratio with height that we see in the Olympus and Ascraeus Mons cases. This latter orbit seems to have a preferred axis in the east–west direction which is not present in the Olympus Mons map. Yet another behavior is observed on Arsia Mons, where the caldera is more depleted than its surroundings and the enrichment has the shape of a ring over the highest part of the mountain. The enrichment ratio is also quite different. In Fig. 6 the change in mixing ratio between the valley and the summit is almost one order of magnitude in the case of Olympus and Ascraeus Mons, approximately a factor 6–7 above Arsia Mons and just ∼2.5 for Pavonis

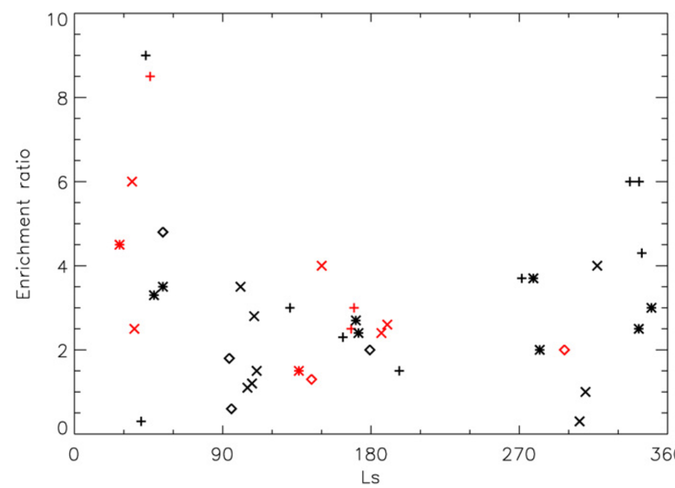

Fig. 8. Enrichment ratio between the bottom of the volcano and the highest part of each orbit against L_s. The different symbols identify the volcanoes as in Fig. 2. The red symbols mark the orbits which show significant enrichment structures and should belong to the enriched group, even when they exhibit an enrichment ratio <2.

Mons. Generally, the mixing ratio trend shows no significant difference between the four Tharsis volcanoes. However, there are hints that Pavonis Mons, the shortest volcano of the four, has on average the smallest degree of enrichment ratio, and Olympus Mons, the tallest one, the largest. Fig. 6 also shows that OMEGA's spatial resolution is high enough to resolve secondary details on top of the main trend. For example, in Fig. 6a the mixing ratio maxima from a crescent shape in the eastern part of the peak; the aforementioned east–west axis in Fig. 6b has a peculiar plumes-like structure; the ring of enrichment of the Arsia Mons retrieval is a structure in itself, and in addition we can notice that it has a clear maximum on the south-western side of the summit. In this paper we will focus mainly on the general behavior, regarding especially the seasonal and diurnal trends, omitting the detailed analysis of the structures of individual orbits.

The enrichment ratio is plotted against season and local solar time in Figs. 8 and 9, respectively. The red symbols in Fig. 8 indicate the orbits with structures. In both plots the data are quite scattered but we can notice some trend. The atmosphere above the volcanoes tends to have the maximum enrichment around

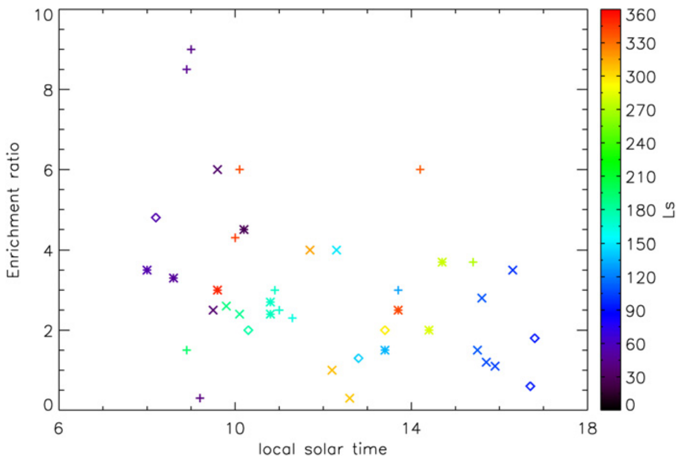

Fig. 9. Enrichment ratio between the bottom of the volcano and the highest part of each orbit against the local solar time. The color labels the L_s of the orbit and the symbol identifies the volcano as in Fig. 2.

the spring equinox ($L_s = 0°$). The enrichment ratio drops from ∼4.7 in the northern spring ($L_s = 0°$–$90°$) to around 2 in summer and autumn ($L_s = 90°$–$200°$) and then increases again in winter, with an average of 3.2 for $L_s = 270°$–$360°$ (4.4 if we restrict the average to the orbits in the late northern winter, $L_s = 330°$–$360°$). More in detail, the enrichment ratio has a minimum in the early northern summer and raises slightly in the course of the summer. Due to the scattering of the results, this is just a tentative conclusion. However, this is supported by the fact that five out of the eleven orbits with an enrichment ratio <2, which can be considered a sort of threshold for the presence of a water enrichment on a volcano, have L_s between 90° and 120°. This behavior can however be due also to a diurnal effect. In fact, this is the only group of orbits observed in the middle–late afternoon. Fig. 9 shows the diurnal trend. All the orbits with enrichment ratio >4 but one are observed before 10:30 A.M. These orbits belong also to the same period of the year, around the northern spring equinox. On the contrary, all the early morning orbits observed in summer have enrichment ratio around 2. From the plot, it seems that in northern winter and spring the enrichment is particularly strong in the morning and decreases in the course of the day, while during the summer the level of enrichment does not show any significant diurnal change.

4.2. Saturation level

The altitude of the atmospheric layer where saturation sets in (Fig. 3) is another output of our retrievals. We computed the average height of saturation level above the surface for six intervals of surface altitude (<0, 0–5, 5–8, 8–11, 11–14, and >14 km—not all the orbits have data points in all the six bins). The saturation level above the volcano (11–14 km bin) is on average ∼3 km closer to the surface than that above the valley (0–5 km). However, the seasonal and diurnal trends are similar for all altitudes, so we present here only the results for the 5–8 km range and we consider it representative for the whole volcano. Figs. 10 and 11 display the seasonal and the diurnal behavior.

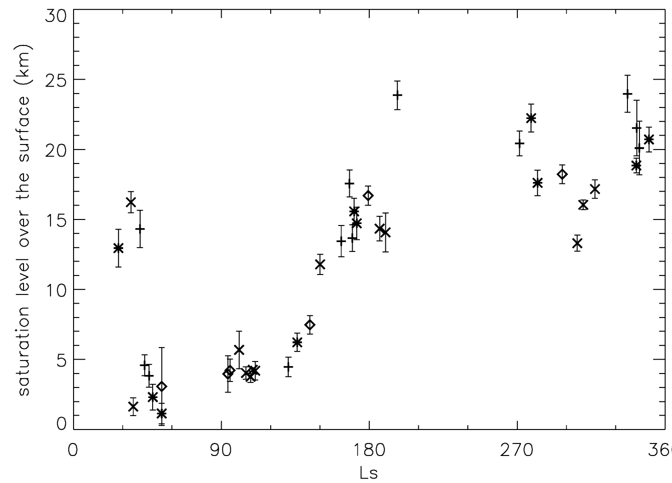

Fig. 10. Average height of saturation level in the 5–8 km surface altitude range against season (L_s). The error bars represent the standard deviation from the average and the symbols identify the volcano as in Fig. 2.

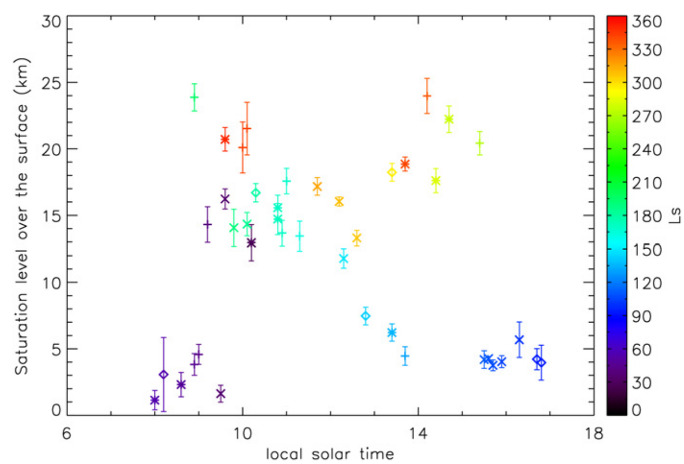

Fig. 11. Average height of saturation level for each orbit in the 5–8 km altitude range against solar time. The color code indicates the L_s and the symbol the volcano.

The most evident feature of the seasonal plot is the minimum at $L_s = 50°$–$110°$, due to low atmospheric temperatures around aphelion. The saturation level falls quite abruptly in the middle of the northern spring at $L_s \approx 45°$ and rises again more gradually during the middle northern summer ($L_s = 130°$–$150°$). There are also hints of a secondary minimum at $L_s \approx 310°$. The general picture is consistent with earlier observations of the global behavior of water vapor saturation at low latitudes (Clancy et al., 1996; Titov, 2002). From Fig. 11 we can also discern a diurnal trend. The saturation level has a minimum in the early morning, rises during the day and then decreases again in the late afternoon. We must be extremely careful though, because there can be a selection bias due to seasonal effects. In fact, the early morning and the late afternoon orbits are also the closest to aphelion. Season seems indeed to play some role on the diurnal behavior of the saturation level. In the northern spring and summer orbits the saturation level has a maximum around 10 and 12 A.M. then decreases steadily, so that at 2 P.M. it has already the same height of the late afternoon. The saturation level is instead more or less constant during the day in northern winter. The coverage of our sample, however, is still too limited to trace a more defined diurnal and seasonal evolution of water vapor saturation.

4.3. Column density

We now analyze the results in terms of column density, which is computed using Eq. (7). Column density is particularly appropriate to represent observations of water vapor in the near-IR spectral range, because it includes both the information on mixing ratio and the saturation level. Fig. 12 shows the column density maps for the same orbits displayed in Fig. 6. Column density decreases by a factor of ∼4 from the valley to the summit of Olympus Mons and only ∼2 for Arsia Mons, while it is almost constant in the Ascraeus Mons map and it has a patchy pattern on Pavonis Mons.

The column density pattern on Olympus Mons is due to the low saturation level over the volcano. In this case, water vapor is confined in a shallow layer just up to ≈1 km above the surface, therefore the vast majority of the atmosphere gives a null contribution to the integral in Eq. (7) and the column density is correspondingly low. On the plains the saturation height is instead around 5 km, still close to the surface but high enough to return a significant value for column density. This is a common situation in the orbits around aphelion. In general, however, one should expect a more significant decrease in column density along the flanks of the mountains. To explain this statement we consider a simple scenario in which both saturation level and mixing ratio below it are constant in the observed region. This is an extreme schematization of water vapor as passive tracer, when its distribution is spatially homogeneous and independent of the topography. Under this assumption Eq. (7) becomes

$$W \approx \frac{m_v}{g\langle M\rangle} f_{\mathrm{H_2O}}(p_0 - p_{\mathrm{sat}}) = \frac{m_v}{g\langle M\rangle} p_0 f_{\mathrm{H_2O}}\big(1 - \exp(-z_{\mathrm{sat}}/H)\big), \quad (8)$$

where we used the hydrostatic equilibrium with no H_2O above the saturation level and $H \approx 10$ km is the atmospheric scale height. In this case H_2O column density is proportional to the surface pressure and the predicted valley-to-summit column density ratio is ∼5, a value which is rarely reached in our orbits. Therefore, the observed column density variations are not consistent with this simple model, suggesting that atmospheric water can be hardly considered just as a passive tracer. The possible scenarios are analyzed in detail in the next section.

5. Discussion and conclusions

We have presented the results of self-consistent retrievals for H_2O mixing ratio, column density and altitude of saturation level over the four Tharsis volcanoes using the OMEGA imaging spectrometer onboard Mars Express. The survey covers more than one martian year in different times of the day, from early morning (8 A.M.) to 5 P.M. The most interesting result is the observed behavior of the water vapor mixing ratio below the saturation level. For most of the year and of the day water vapor concentrates over the summit of the volcanoes more than on the nearby plains, resulting in a certain degree of enrichment (Fig. 6). The transition between the valley and the top of the mountain is usually gradual, and water vapor mix-

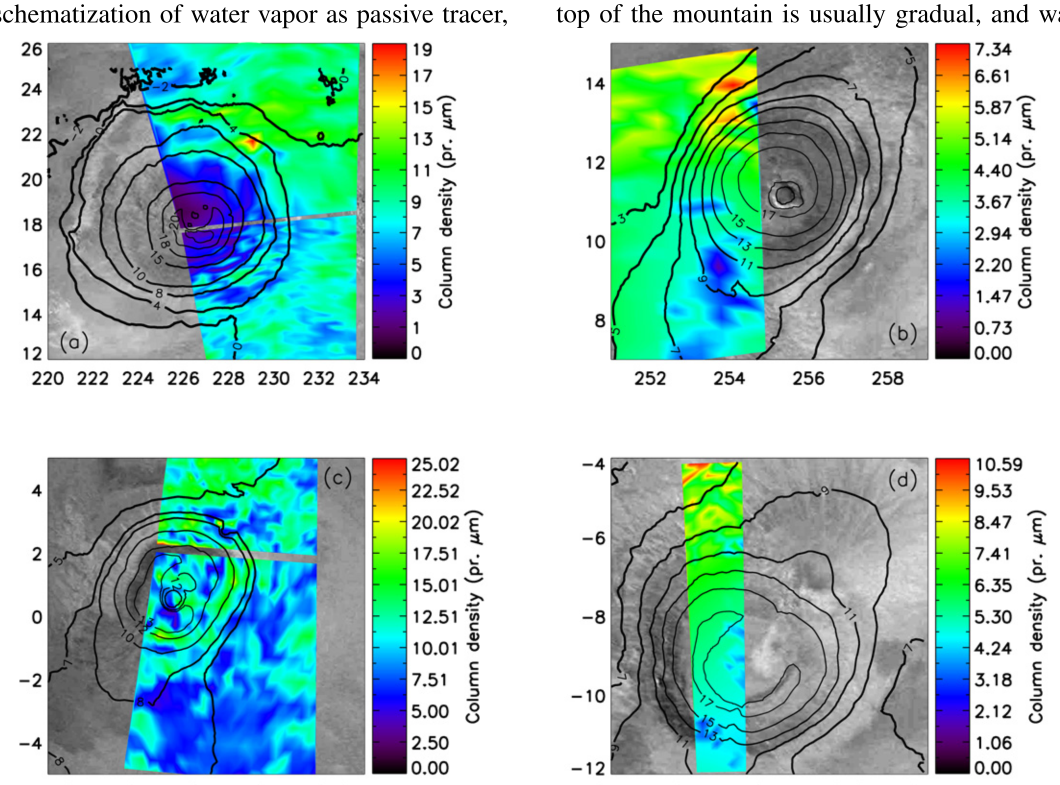

Fig. 12. Column density maps for the same orbits as in Fig. 6.

ing ratio is positively correlated with altitude in most of the orbits. In some cases the presence of structures of high mixing ratio with different shapes substitutes or is superimposed on this smooth enhancement (Fig. 7). Although interesting for its physical implications, a detailed study of these enrichment structures is quite delicate because of the high relative error on mixing ratio, and it is beyond the scope of this paper.

We quantify the enrichment by the enrichment ratio defined in Section 4.1. If we consider an enrichment ratio of 2 as the threshold between the enriched and the non-enriched orbits, we see that 32 orbits out of 41 ($\sim$75%), can be considered enriched. In this group the two orbits with enrichment ratio <2 but with an enrichment structure are also included (see Fig. 8). Twelve orbits out of these 32 present enrichment structures. Of the remaining non-enriched 9 orbits, 5 are concentrated in the early northern summer. Most of the orbits have an enrichment factor between 2 and 4. All the orbits which show an enrichment ratio >4 were observed around the northern spring equinox, between $L_s = 330°–60°$. The vast majority of these orbits was also observed before 10:30 A.M. All these results suggest a seasonal driver for the enrichment, possibly coupled with a diurnal effect. Unfortunately, the seasonal and the diurnal influence cannot be entirely disentangled, because the L_s and the local time of the observations are related through the evolution of Mars Express orbit. The data of the next martian year, during which each martian day is going to be observed at a different local hour, will permit to discern the relative importance of these two parameters on the enrichment.

The lack of correlation between the seasonal behavior of the enrichment and the seasonal cycle of ice clouds is another confirmation that the influence of ice clouds on the retrieval is minor. In fact, ice clouds have their maximum of activity during the northern summer (Benson et al., 2003), while we found that the enrichment is present during the whole year and actually has a minimum in the early northern summer. Figs. 5–7 seem to rule out also the possibility that ice clouds are the main factor behind spatial inhomogeneities in the distribution of water vapor mixing ratio as the "enrichment structures." For example, the ice cloud in Fig. 5d has a north–south orientation while the plumes-like structures in Fig. 6b have an east–west axis. Similarly, Fig. 5b has no clouds, but the corresponding mixing ratio map (Fig. 7a) shows a strong structure on the south-western flank of the volcano.

What are the physical processes behind the observed peculiarities? Similar ISM-Phobos results were explained by an enhanced surface–atmosphere water exchange on the flanks of the volcanoes due to different properties of the regoliths between the summit of the volcanoes and the valley (Titov et al., 1994). In this model atmospheric water amount is governed by the desorption from the regolith and/or frost sublimation, and water vapor is mainly confined in a few kilometer thick boundary layer. This makes column density dependent only on regolith properties and surface temperature, but not on surface pressure. This mechanism explains a mixing ratio enrichment up to a factor of several units, which is quite consistent with the majority of our orbits. However, the outgassing from the regolith cannot explain entirely the observed behavior. In fact, we would expect stronger diurnal variations, depending on the characteristic time of outgassing of the regoliths under solar illumination. We also would expect higher enrichment ratio in the orbits observed in the morning and close to the perihelion, because the higher solar flux implies a more efficient desorption mechanism, while Fig. 9 shows the opposite situation.

Most probably, water vapor transport by mesoscale atmospheric circulation also plays a role in the maintenance of the observed pattern. The Tharsis plateau is inside the region influenced by the cross-equatorial Hadley cell which dominates the tropical martian circulation (Haberle et al., 1982). This single cell is stronger and wider during the solstices, the northern winter solstice in particular. The low-level flow associated to the Hadley circulation is sufficiently intense to create winds reaching, on the Tharsis region, velocities of 25–30 $\mathrm{m\,s^{-1}}$ during the solstices (Joshi et al., 1997). The most evident effect of these jets is the transport of dust, which manifests through the presence of various kinds of aeolian features, but most probably they carry also a certain amount of water vapor. The effects of topography on the circulation in the vicinity of the volcanoes cannot however be neglected. An analysis of the wind streaks in Tharsis observed by the Viking Orbiter established that the streak pattern is controlled by slope winds (Lee et al., 1982), and also the modeling of the Hadley circulation through GCMs shows that its lower branch is strongly regulated by topographic features (Greeley et al., 1993). Thus, the extreme topography of the Tharsis region strongly affects atmospheric circulation. The global circulation which instates the equatorial Hadley cell can play some role in the transport of water vapor, but the dominant influence is to be assigned to the local circulation. This conclusion seems to be confirmed by the fact that we observe the maximum of enrichment around the spring equinox, when the cross-equatorial Hadley cell is at its weakest. For this reason, reliable insights can be given only by mesoscale models. Up to now, only Rafkin et al. (2002) and Michaels et al. (2006) studied the mountain circulation with a mesoscale model. The results are quite remarkable regarding water vapor transport. During the day, strong upslope flows, due to a combination of thermal effects with mountain gravity waves, set up and act as a "pump" that moves large quantities of water along the slopes of the volcanoes. The upflows extend from the base of the mountain to altitudes greater than 40 km. This mechanism can thus redistribute water vapor from the valley to the summit of the volcano and, together with the lowering of the condensation level, generate the enrichment. The lower degree of enrichment during early northern summer afternoons is more difficult to explain, also because Michaels et al. (2006) do not discuss the seasonal behavior of their mesoscale model. We can suppose that in early morning the strong thermal forcing due to the onset of the solar heating starts and ignites the upflows as usual, creating the enrichment. As the day progresses, however, the low altitude of the saturation level can inhibit the local circulation. This effect, acting together with the condensation level close to the surface, can effectively deplete the atmosphere over the volcanoes of water vapor.

The two processes, surface–atmosphere exchange and atmospheric transport, can also act simultaneously and both can contribute to the enrichment phenomenon. For example, the strong enrichment in the early morning that we explained above using upslope water transport, can be enhanced by regolith desorption. Correspondingly, in the late afternoon the adsorption of water into the regolith can already have started and can play a role to lower the enrichment ratio, especially if the regolith on the volcano summit is more efficient in the exchange with the atmosphere or if the low altitude of the saturation level maintains the water vapor closer to the surface, as happens around the aphelion. In order to determine their relative contribution and in general to have a better understanding of the phenomenon of enrichment, however, a detailed model that includes both mechanisms must be developed. New observations from OMEGA/MEx and CRISM and MCS experiments onboard the Martian Reconnaissance Orbiter (MRO) (Zurek and Smrekar, 2007) are expected to give new insights on the spatial and vertical distribution of atmospheric water in the vicinity of the martian volcanoes.

Acknowledgments

We wish to thank the ISSI (International Space Science Institute) in Bern (Switzerland) for supporting the Forum "Water in Mars' Atmosphere: Comparison of Recent Data Sets," and Alexander Rodin and an anonymous reviewer for their insightful and useful comments.

References

Benson, J., Bonev, B., James, P., Shan, K., Cantor, B., Caplinger, M., 2003. The seasonal behavior of water ice clouds in the Tharsis and Valles Marineris regions of Mars: Mars Orbiter Camera Observations. Icarus 165, 34–52.

Benson, J., James, P., Cantor, B., Remigio, R., 2006. Interannual variability of water ice clouds over major martian volcanoes observed by MOC. Icarus 184, 365–371.

Bibring, J.-P., Soufflot, A., Berthé, M., Langevin, Y., Gondet, B., Drossart, P., Bouyé, M., Combes, M., Puget, P., Semery, A., Bellucci, G., Formisano, V., Moroz, V., Kottsov, V., Bonello, G., Erard, S., Forni, O., Gendrin, A., Manaud, N., Poulet, F., Poulleau, G., Encrenaz, T., Fouchet, T., Melchiorri, R., Altieri, F., Ignatiev, N., Titov, D., Zasova, L., Coradini, A., Capacionni, F., Cerroni, P., Fonti, S., Mangold, N., Pinet, P., Schmitt, B., Sotin, C., Hauber, E., Hoffmann, H., Jaumann, R., Keller, U., Arvidson, R., Mustard, J., Forget, F., 2004. OMEGA: Observatoire pour la Minéralogie, l'Eau, les Glaces et l'Activité. In: Mars Express: The Scientific Payload. ESA SP-1240, pp. 37–49.

Clancy, R., Grossman, A., Wolff, M., James, P., Rudy, D., Billawala, Y.N., Sandor, B., Lee, S., Muhleman, D., 1996. Water vapor saturation at low altitudes around Mars aphelion: A key to Mars climate? Icarus 122, 36–62.

Encrenaz, T., Lellouch, E., Paubert, G., Gulkis, S., 2001. The water vapor vertical distribution on Mars from millimeter transitions of HDO and $H_2^{18}O$. Planet. Space Sci. 49, 731–741.

Encrenaz, T., Melchiorri, R., Fouchet, T., Drossart, P., Lellouch, E., Gondet, B., Bibring, J.-P., Langevin, Y., Titov, D., Ignatiev, N., Forget, F., 2005. A mapping of martian water sublimation during early northern summer using OMEGA/Mars Express. Astron. Astrophys. 441, L9–L12.

Farmer, C., Davies, D., Holland, A., Laporte, D., Doms, P., 1977. Mars—Water vapor observations from the Viking orbiters. J. Geophys. Res. 82, 4225–4248.

Fedorova, A., Rodin, A., Baklanova, I., 2004. Seasonal cycle of water vapor in the atmosphere of Mars as revealed from the MAWD/Viking 1 and 2 experiment. Solar System Res. 38, 421–433.

Fedorova, A., Korablev, O., Bertaux, J.-L., Rodin, A., Kiselev, A., Perrier, S., 2006. Mars water vapor abundance from SPICAM IR spectrometer: Seasonal and geographic distributions. J. Geophys. Res. (Planets) 111 (E10), 9–26.

Forget, F., Hourdin, F., Fournier, R., Hourdin, C., Talagrand, O., Collins, M., Lewis, S., Read, P., Huot, J.-P., 1999. Improved General Circulation Models of the martian atmosphere from the surface to above 80 km. J. Geophys. Res. 104, 24155–24176.

Grassi, D., Fiorenza, C., Zasova, L., Ignatiev, N., Maturilli, A., Formisano, V., Giuranna, M., 2005. The martian atmosphere above great volcanoes: Early Planetary Fourier Spectrometer observations. Planet. Space Sci. 53, 1053–1064.

Greeley, R., Skypeck, A., Pollack, J., 1993. Martian aeolian features and deposits—Comparisons with general circulation model results. J. Geophys. Res. 98, 3183–3196.

Gurwell, M., Bergin, E., Melnick, G., Ashby, M., Chin, G., Erickson, N., Goldsmith, P., Harwit, M., Howe, J., Kleiner, S., Koch, D., Neufeld, D., Patten, B., Plume, R., Schieder, R., Snell, R., Stauffer, J., Tolls, V., Wang, Z., Winnewisser, G., Zhang, Y., 2000. Submillimeter wave astronomy satellite observations of the martian atmosphere: Temperature and vertical distribution of water vapor. Astrophys. J. 539, L143–L146.

Haberle, R., Leovy, C., Pollack, J., 1982. Some effects of global dust storms on the atmospheric circulation of Mars. Icarus 50, 322–367.

Hartmann, W., 1978. Mars—Topographic control of clouds, 1907–1973. Icarus 33, 380–387.

Hunt, G., Pickersgill, A., James, P., Johnson, G., 1980. Some diurnal properties of clouds over the martian volcanoes. Nature 286, 362–364.

Jakosky, B., Farmer, C., 1982. The seasonal and global behavior of water vapor in the Mars atmosphere—Complete global results of the Viking atmospheric water detector experiment. J. Geophys. Res. 87, 2999–3019.

Joshi, M., Haberle, R., Barnes, J., Murphy, J., Schaeffer, J., 1997. Low-level jets in the NASA Ames Mars general circulation model. J. Geophys. Res. 102, 6511–6524.

Lee, S., Thomas, P., Veverka, J., 1982. Wind streaks in Tharsis and Elysium—Implications for sediment transport by slope winds. J. Geophys. Res. 87, 10025–10041.

Mauersberger, K., Krankowsky, D., 2003. Vapor pressure above ice at temperatures below 170 K. Geophys. Res. Lett. 30, doi:10.1029/2002GL016183. 21-1.

Melchiorri, R., Encrenaz, T., Fouchet, T., Drossart, P., Lellouch, E., Gondet, B., Bibring, J.-P., Langevin, Y., Schmitt, B., Titov, D., Ignatiev, N., 2007. Water vapor mapping on Mars using OMEGA/Mars Express. Planet. Space Sci. 55, 333–342.

Michaels, T., Colaprete, A., Rafkin, S., 2006. Significant vertical water transport by mountain-induced circulations on Mars. Geophys. Res. Lett. 33, doi:10.1029/2006GL026562. 16201.

Rafkin, S., Sta. Maria, M., Michaels, T., 2002. Simulation of the atmospheric thermal circulation of a martian volcano using a mesoscale numerical model. Nature 419, 697–699.

Rothman, L., Jacquemart, D., Barbe, A., Benner, D., Birk, M., Brown, L., Carleer, M., Chackerian, C., Chance, K., Coudert, L., Dana, V., Devi, V., Flaud, J., Gamache, R., Goldman, A., Hartmann, J., Jucks, K., Maki, A., Mandin, J., Massie, S., Orphal, J., Perrin, A., Rinsland, C., Smith, M., Tennyson, J., Tolchenov, R., Toth, R., Vander Auwera, J., Varanasi, P., Wagner, G., 2005. The HITRAN 2004 molecular spectroscopic database. J. Quant. Spectrosc. Radiat. Trans. 96, 139–204.

Smith, M., 2002. The annual cycle of water vapor on Mars as observed by the Thermal Emission Spectrometer. J. Geophys. Res. (Planets) 107, doi:10.1029/2001JE001522. 25-1.

Titov, D., 2002. Water vapor in the atmosphere of Mars. Adv. Space Res. 29, 183–191.

Titov, D.V., Haus, R., 1997. A fast and accurate method of calculation of gaseous transmission functions in planetary atmospheres. Planet. Space Sci. 45, 369–377.

Titov, D., Moroz, V., Grigoriev, A., Rosenqvist, J., Combes, M., Bibring, J.-P., Arnold, G., 1994. Observations of water vapory anomaly above Tharsis volcanoes on Mars in the ISM (Phobos-2) experiment. Planet. Space Sci. 42, 1001–1010.

Zurek, R., Smrekar, S., 2007. An overview of the Mars Reconnaissance Orbiter (MRO) science mission. J. Geophys. Res. (Planets) 112 (E11), doi:10.1029/2006JE002701. 5.